SIZING AND TOPOLOGY DESIGN OF AN AEROELASTIC WINGBOX UNDER UNCERTAINTY

Bret K. Stanford[1] and Satadru Roy[2]

[1]NASA Langley Research Center
Hampton, Virginia 23681 USA
bret.k.stanford@nasa.gov

[2]Purdue University
West Lafayette, Indiana USA
roy10@purdue.edu

Keywords: topology optimization, uncertainty, wingbox, aeroelasticity

Abstract: The goals of this work are to use a nested optimizer to conduct simultaneous sizing (inner level) and topology (outer level) design of a wingbox, considering uncertainties in the safety factors used to define the aeroelastic constraints. These uncertainties, propagated via sampling-driven polynomial chaos, are explicitly introduced at the inner level of the method, during gradient-based sizing optimization, resulting in a stochastic optimal sizing distribution. Measures of robustness in the total structural mass are then passed to the outer level, where a global optimizer evolves the topology parameters. The results demonstrate design choices needed to improve robustness in the face of uncertain safety factors, and the various physical mechanisms driving this process.

1 INTRODUCTION

Previous work by the authors [1, 2] has considered the aeroelastic design optimization of a transport wingbox for the Common Research Model [3]. This work seeks to locate the optimal layout/topology of ribs and stringers within the wingbox, and simultaneously size each of these components in addition to each skin panel. The goal of the design process is to minimize structural weight, pursuant to constraints on stress and buckling across a series of trimmed static aeroelastic load cases. The optimization problem is a mixed-integer-nonlinear-programming problem (MINLP), as some of the design variables (i.e., the number of ribs) are integer variables, whereas others (i.e., the web thickness of each rib) are continuous variables. Such MINLP problems are very difficult to solve, particularly if there are a large number of design variables, as considered in Refs. [1] and [2].

The interdependencies between sizing and layout design variables are very strong: decreasing the number of ribs in the wingbox (for example) in order to reduce structural weight, will increase the acreage of the concomitant skin panels bordered by those ribs, and force the panel thickness (and therefore structural weight) to be *increased* to prevent buckling during loading. In order to properly capture these coupled design spaces, the two types of design variables (sizing and layout/topology) should be optimized simultaneously, but MINLP schemes will scale poorly for larger design spaces. A reasonable alternative is a nested algorithm, considered in Refs. [4], [5], and [6], where the layout variables are optimized with a dedicated nongradient-based global optimizer in the outer level, and the sizing variables are optimized with a dedicated

gradient-based optimizer in the inner level. The choice of global optimizer is a crucial one; nongradient-based optimizers are very expensive in general, but in this work each wingbox layout considered by the global optimizer spawns an entire gradient-based sizing optimization process at the nested level. Ref. [1] demonstrates the viability of the Bayesian infill MISO-CPTV scheme of Ref. [7] for this role; Ref. [2] compares various other infill schemes.

The point of departure from prior work, considered in this paper, is design under uncertainty. As summarized in Refs. [8] and [9], design under uncertainty can be roughly divided into two categories: reliability-based design optimization (RBDO), and robust design optimization (RDO). The former is concerned with unlikely scenarios with catastrophic consequences that occur in the tails of a probability density function (PDF): replacing the safety factor of a design constraint with some limiting probability of failure, for example. RDO, on the other hand, is concerned with likely scenarios of noncatastrophic consequences (moderate off-design performance degradation, for example) that occur near the mean of a PDF. RDO may seek designs that sacrifice some nominal design performance for improved robustness (e.g., decreased variance).

This work will discuss one such technique by which uncertainties can be included in the aforementioned nested wingbox design problem, and demonstrate how the strong interdepencies between sizing and layout design spaces shift, when exposed to these uncertainties. Specifically, the safety factors (SF) used to drive the sizing design process are considered to be random. Two safety factors are considered here, both nominally set to 1.5: the safety factor associated with the von Mises stress envelope during aeroelastic maneuvers, and the safety factors associated with skin buckling. Appropriate values of SF are highly uncertain, in terms of the ideal trade-off between conservatism and structural performance, particularly for the linear skin buckling computations [10] performed here.

The idea of uncertain safety factors is not new: see Ref. [11] for discussion of a "stochastic safety factor", or Ref. [12] for the related idea of a "probabilistic sufficiency factor". In these works, probabilistic inputs are propagated through a system, and output reliability is interpreted as a safety factor. The idea in the current work will be to propagate the uncertain safety factors themselves through the sizing optimization process (the probabilistic inputs in this case are the safety factors, or the failure boundaries), resulting in an uncertain optimal sizing distribution along the wingbox components. In the random event that the safety factors are larger than 1.5, then the thickness of the various members will be higher (i.e., heavier), and vice-versa. The nested algorithm described above can then be introduced, in order to identify wingbox topologies whose sizing is less susceptible to these uncertainties (i.e., more robust). It is noted that the work proposed here does not fit cleanly into either the RBDO or the RDO ideas summarized above, but instead has elements of both owing to the nested element of the algorithm. RBDO-based concepts are represented in the fact that the failure boundaries are assumed to be stochastic, while the outer-level design problem focuses on ideas of robustness, as would be done in RDO.

This work is organized as follows: first, a deterministic nested topology/sizing optimization process is reviewed. Next, this optimal deterministic design is post-processed to include uncertainties in the aeroelastic safety factors, to demonstrate the uncertain optimal sizing distribution that ensues. Finally, a complete optimization process considering uncertainty is undertaken, in order to locate the wingbox topology that improves the robustness of the system due to uncertain safety factors.

2 DETERMINISTIC OPTIMIZATION

Ignoring uncertainties for now, the nested wingbox optimization scheme operates as follows. Design variables are segregated into topology/layout variables, $\boldsymbol{x}_{topology}$, and sizing variables, $\boldsymbol{x}_{sizing}$. The baseline, "empty" wingbox, shown on the left of Fig. 1, is composed of the skins, stiffened spars, a close-out rib, and a rib located at the trailing edge break: these topological features are constant. From this starting point, the members of $\boldsymbol{x}_{topology}$ define the number and spacing of the inboard ribs, the number and spacing of the outboard ribs, the number, spacing, and orientation of the upper stringers, and the number, spacing, and orientation of the lower stringers (10 design variables total). Four of these design variables are integers; the remaining six are continuous, but their design space may not be smooth enough for the use of gradient-based optimization.
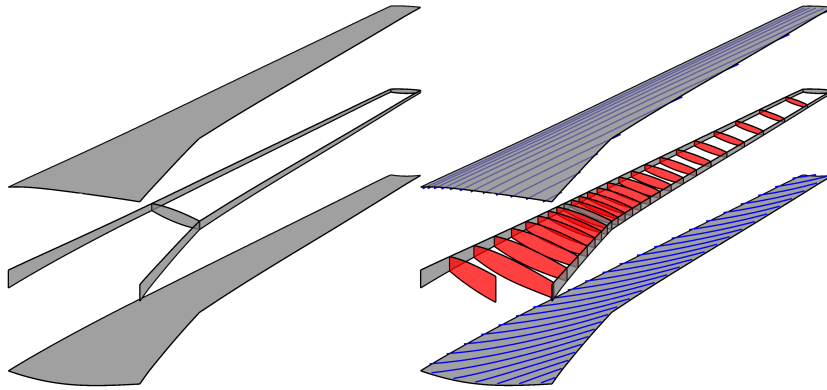

Figure 1: Sample wingbox topology.

Therefore, a nongradient-based global optimizer is used to handle $\boldsymbol{x}_{topology}$, namely an infill-based surrogate optimizer. An initial population of $\boldsymbol{x}_{topology}$ is constructed via Latin hypercube sampling (LHS), a radial basis function (RBF) is fit to this data, and the surrogate model is used to identify an infill point: i.e., the next topological design worth exploring. Several different ideas may be used to identify the infill point; the Coordinate Perturbation (CP) method [13] is used here, as adapted for MINLP problems in Ref. [7]. Finally, for each wing layout/topology considered by the global optimizer, the layout is frozen, and a complete gradient-based aeroelastic optimization of $\boldsymbol{x}_{sizing}$ is conducted. This is done by splitting the upper skin, lower skin, leading spar, trailing spar, and internal ribs each into 5 zones, leaving 25 total. Within each zone, the thickness of each shell member (t), the thickness of the stiffeners attached to these shells (t_s), and the height of the stiffeners (h_s), are independently optimized (see Fig. 2), leaving 75 total sizing design variables.

The gradient-based sizing optimizer is able to find the $\boldsymbol{x}_{sizing}$ that minimizes structural mass for a fixed $\boldsymbol{x}_{topology}$, and also satisfies each aeroelastic constraint. These constraints are formed around four trimmed aeroelastic load cases: a $2.5g$ pull-up maneuver, a $-1g$ push-over, a roll maneuver, and a $2g$ landing load. For each load case, the von Mises stresses are computed for each finite element across the metallic wingbox, and multiplied by a safety factor, k_s, nominally set to 1.5. These von Mises stresses are aggregated into a small number of constraints [14]: one each for the stiffened upper skins, lower skins, ribs, and spars. Next, the first ten buckling eigenvalues are computed for each load case, and multiplied by a second safety factor, k_b, also set to 1.5. These ten eigenvalues are again aggregated into a single constraint.
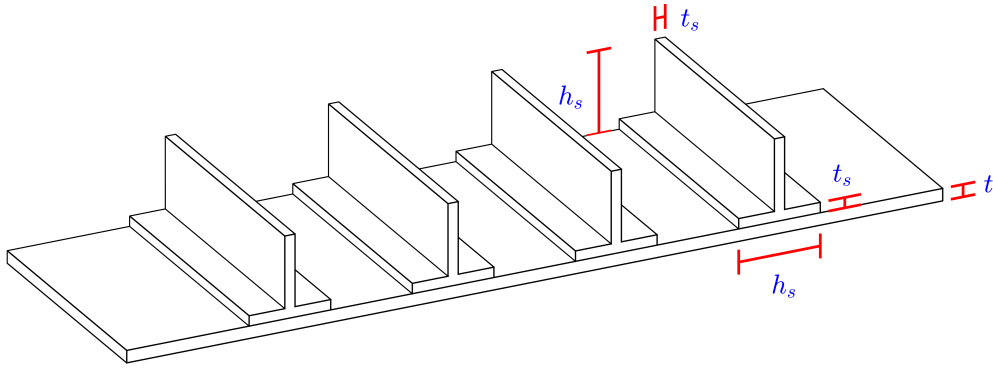
Figure 2: Example T-stiffener geometry.

Upon convergence of the gradient-based sizing optimizer, the optimal structural mass is returned to the global infill-based topology optimizer, for use as the quantitative metric needed to fit the RBF models. As each aeroelastic constraint is satisfied by the sizing optimizer (i.e., set to zero, or otherwise inactive), these constraint values do not need to be returned to the global topology optimizer. The global optimizer uses the performance at the infill point to recompute the RBF across the $x_{topology}$ space, and then selects a new infill point for consideration. The algorithmic steps can be summarized as:

1. Generate an initial population of $x_{topology}$ designs using LHS.
2. For each member of $x_{topology}$, conduct the complete gradient-based optimization of x_{sizing}, and return the optimal structural mass, f.
3. Fit f with a radial basis function (RBF) surrogate model across the $x_{topology}$ design space.
4. Use the surrogate model to find an infill point: i.e., the next topological design worth exploring.
5. For the new $x_{topology}$ infill point, conduct the complete gradient-based optimization of x_{sizing}, and return the optimal structural mass, f.
6. Recompute the surrogate model with this new data point included.
7. Return to step 4, and repeat until some convergence criteria is attained.

Convergence of this process is shown in Fig. 3. The best available objective among the set (including an initial LHS population of 240 designs, and the subsequently computed infill points) at each outer iteration is shown on the left of this figure. The plot starts at 12,690 kg, which is the lightest (after sizing optimization) of the initial LHS designs, and converges to a value of 12,258 kg after 55 outer iterations. The infill points selected by the CP routine are usually successful toward the beginning of the process, in that the selected infill point does lead to a structural mass lighter than any other computed up to that point; toward the end of the process, the infill points are less-frequently successful. It is noted again that each data point on this plot represents a complete sizing-based optimization of the topology. Two examples of this gradient-based optimization are shown on the right of Fig. 3: one for outer iteration 3, where the sizing optimization of the infill point manages to converge to a value superior to the present best objective, and another (iteration 31), where it does not.

The optimal topology and sizing distribution is finally shown in Fig. 4. The thickness of the skins is generally highest near the break in the trailing edge wing geometry, and thins toward the tip. The lower skins are thicker than the upper skins, but the number of stiffeners, and the size of each stiffener attached to the lower skins, is generally less.
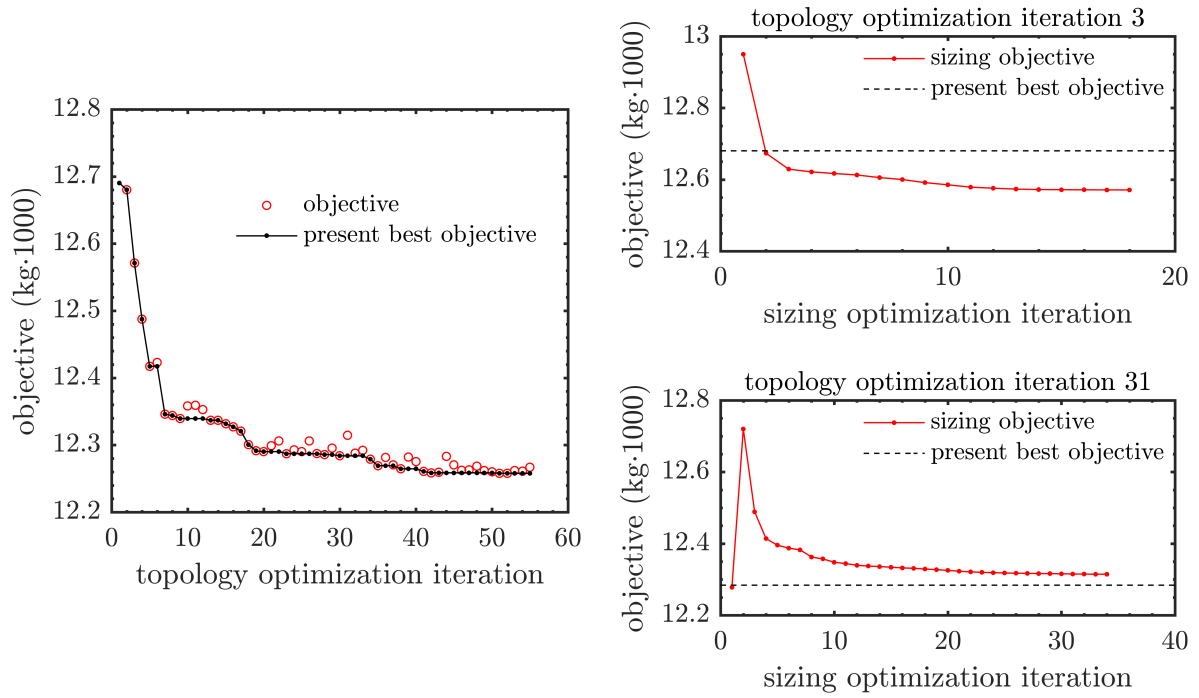
4

Figure 3: Deterministic topology/sizing optimization convergence.

3 UNCERTAINTY ANALYSIS OF THE DETERMINISTIC OPTIMIZATION

Next, the optimal topology found in the previous section is resized via uncertain safety factors, k_s and k_b. Both are assumed to be normally distributed, with a mean of 1.5 and a standard deviation of 0.15. As noted, a random distribution of safety factors will lead to a random distribution of optimal wingbox sizing parameters, since the gradient based optimization is dependent on the SF. Higher SF values will force the sizing optimizer to return structures with higher mass (as the aeroelastic constraints are harder to satisfy), and vice-versa. Uncertainty propagation is accomplished via a nonintrusive polynomial chaos expansion (NIPCE), via a sampling-based (LHS) point collocation [15,16]. This PCE method samples the random variable space via LHS, fits the samples with a surrogate model via assumed basis functions, and then uses the resulting surrogate model to compute statistical moments, probability distribution functions (PDFs), etc.
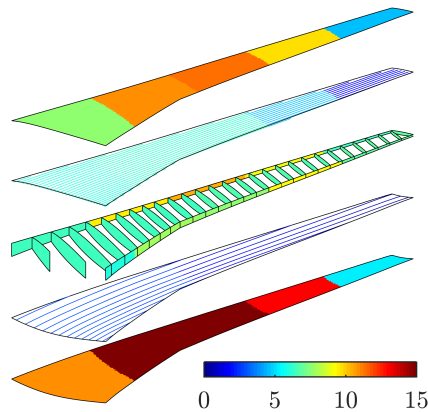

Figure 4: Exploded view of the optimal topology and sizing distribution (equivalent thickness, mm) for the deterministic design.

5

For this work, there are two random variables (k_s and k_b), and a second-order PCE is desired. At least 6 samples across the random variable space are therefore required to compute the basis function coefficients (a total-order expansion of Hermite polynomials [16]), but Ref. [15] recommends an oversampling rate of two, which then requires 12 samples. Each of the 12 samples is shown in Fig. 5, in terms of the sizing parameters found via gradient-based optimization, in response to the safety factors stated in the figure. The topology is frozen across each design in this figure, set to the optimal topology found in the previous section.
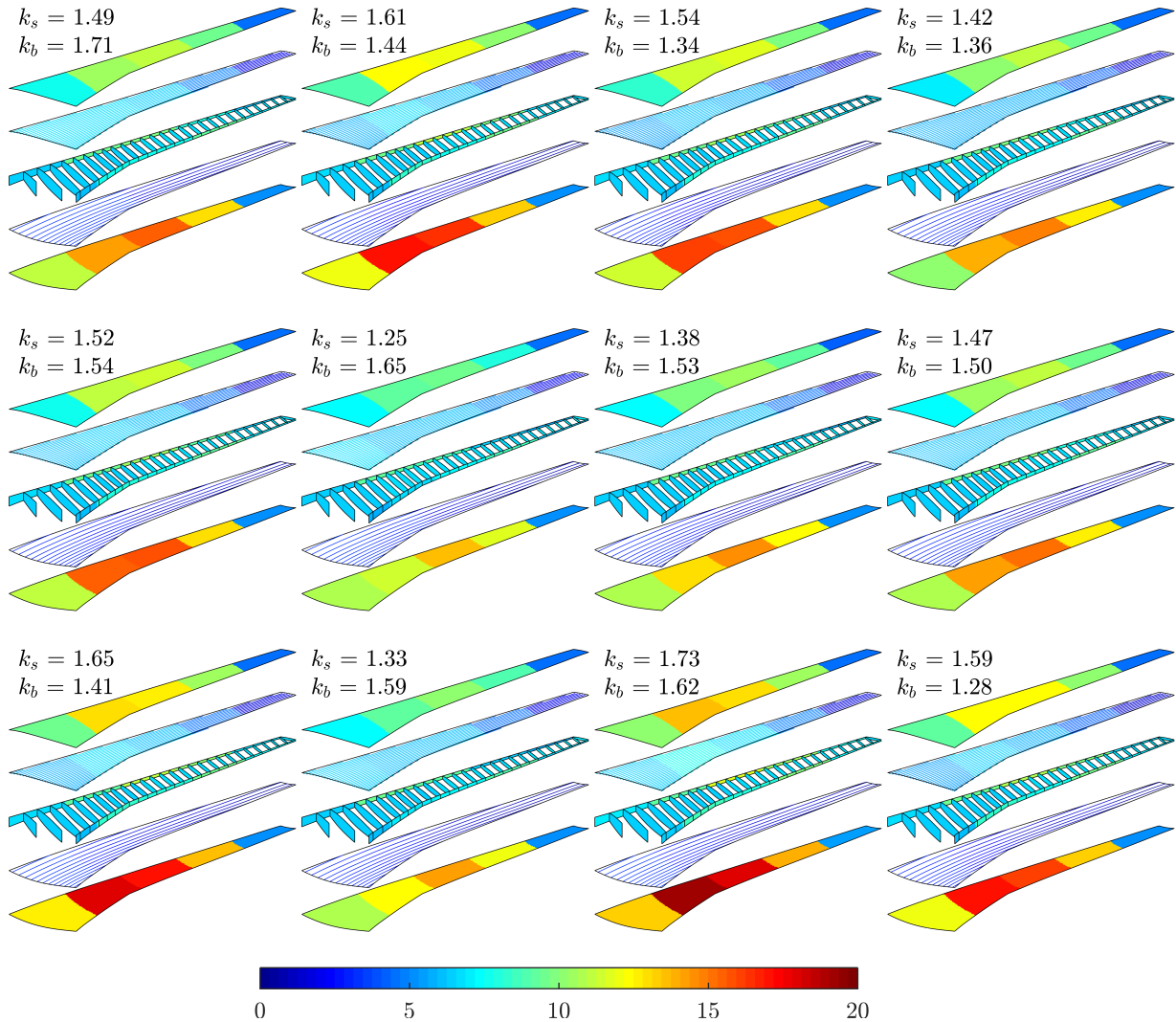

Figure 5: Optimal sizing distributions (equivalent thickness, mm) found for each of the 12 PCE samples, for the deterministically-optimal wingbox topology.

Using the formulas given in Ref. [16], the mean and standard deviation for each sizing design variable is shown in Fig. 6. The mean sizing values, as may be expected, are quite similar to the nominal deterministic values shown in Fig. 4. The standard deviation contour indicates sizing patches that are sensitive to variations in SF; this is largest for the lower skin design patch near the trailing edge break (sizing coefficient of variation, COV, equal to 16.8%), as well as the corresponding patch in the upper skin (COV of 14.7%) and a design patch in the leading spar toward the wingtip (COV of 19.6%). The resulting low-order PCE surrogate can also be used to estimate the PDF via high-volume sampling. This can be done for every sizing design patch in Fig. 6, but for brevity is only shown for the total structural mass. This PDF is skewed

(i.e., nonlinear) toward higher mass values, justifying the use of a second-order PCE. The mean structural mass is 12,446 kg, and the standard deviation is 976 kg. The mean structural mass (12,446 kg) is different from the nominal structural mass (12,258 kg) owing to the nonlinearity of the PDF. Higher structural mass standard deviations would be obtained if the standard deviation of the safety factors was chosen to be higher, and vice-versa.
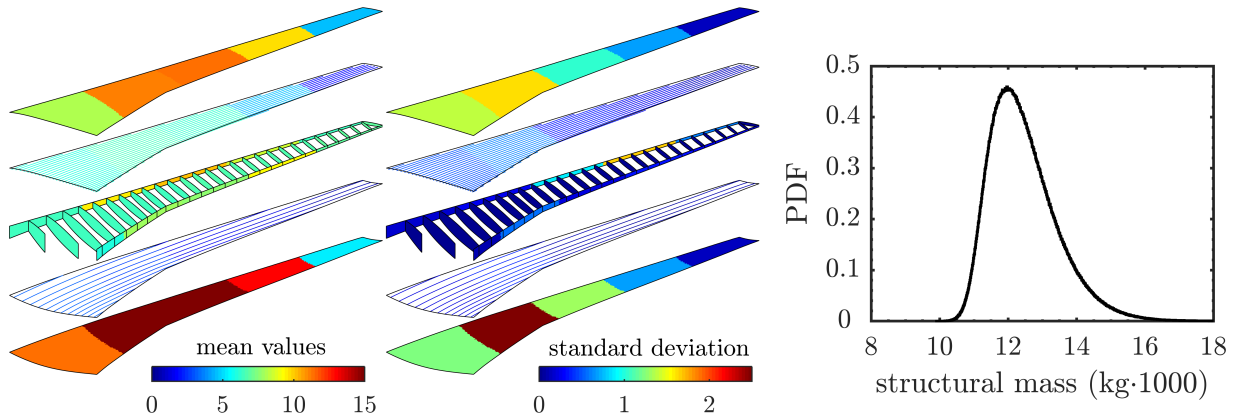

Figure 6: Mean and standard deviation of the sizing distributions (equivalent thickness, mm) found via the 12 PCE samples in Fig. 5, as well as the PDF of the total structural wing mass.

The random stress distributions found from the optimal sizing of Fig. 6, are found in Fig. 7, for the 2.5g pull-up maneuver. Specifically, the von Mises stress is shown, increased via the random SF k_s, and then normalized by the yield stress. The nominal (deterministic) stress field is not shown, but looks quantitatively similar to the mean values. This stress constraint is active (i.e., equal to unity) for several locations throughout the wingbox, and these areas remain active for every instance of k_s: the sizing optimizer will always tune the skin thickness (for example) to bring the local stresses to the failure boundary. As such, the stress variability is low in areas where the stress constraint is active, though the sizing variability (Fig. 6) in these areas is high. The opposite is true in areas where the stress constraint is inactive: stress variability is high, but sizing variability is low.

The principle of fully stressed design [17] would indicate that every component of the wingbox should have an active stress constraint (otherwise it would be too heavy), driving the stress variability in Fig. 7 to near-zero throughout. Other constraints, such as buckling constraints (discussed next), minimum-size constraints, and stiffener geometry constraints, keep the stress constraints from being spatially active throughout, however.

The critical buckling eigenvalue is active for each load case, for every value of the SF k_b: like the stress constraints, the sizing optimizer will always tune the skin thickness (for example) to bring the critical buckling eigenvalue to the failure boundary. As such, the buckling eigenvalue variability is near-zero. Variability in the critical mode shape, for the 2.5g pull-up, is shown in Fig. 8, and appears as periodic lobes in the upper skin near the root, whose wavelength is driven by the local rib pitch. It can be inferred from the figure that the "identity" of the critical buckling mechanism is not a strong function of the safety factors: if it had been, one may have expected disjointed behavior in the buckling variation across the k_s-k_b space, which would have been difficult for the second-order PCE used here to fit. Ref. [18] discusses methods to span PCE's across disjointed parameter spaces, in the context of aeroelastic flutter mechanisms.
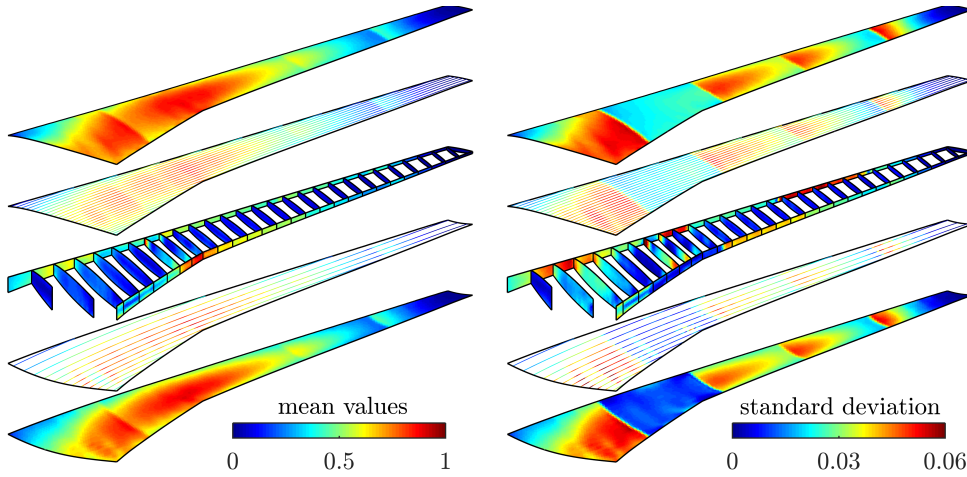
Figure 7: Random normalized von Mises stress distributions, including the safety factor k_s, during the 2.5g maneuver.
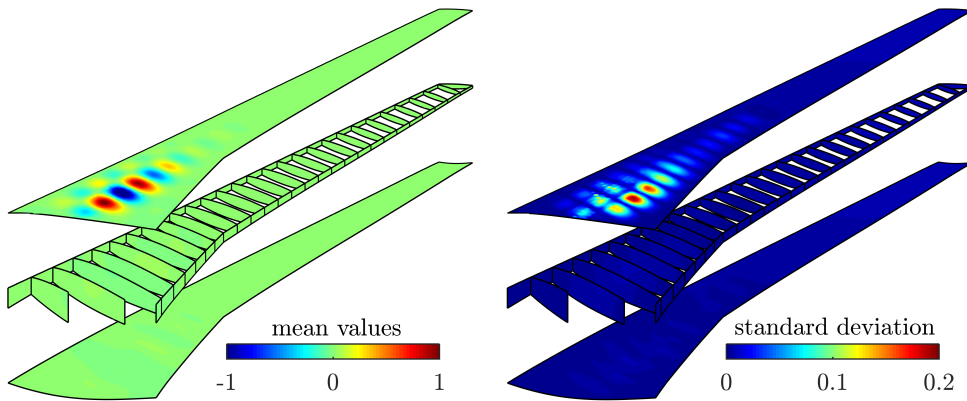

Figure 8: Random critical buckling mode shapes, during the 2.5g maneuver.

4 OPTIMIZATION UNDER UNCERTAINTY

As noted in the previous sections, the nested sizing/topology optimization, run deterministically with both k_s and k_b set to 1.5, is able to drive the structural mass down to 12,258 kg (Fig. 3). Then, the optimal topology is resized under stochastic safety factors (Fig. 6) resulting in a mean structural mass of 12,446 kg, and standard deviation of 976 kg. The goals of this section are to rerun the nested sizing/topology optimization, but instead of minimizing deterministic structural mass, we minimize some linear combination of the mean structural mass and the standard deviation of the structural mass. The computational cost of this exercise is much higher: previously, each infill point identified by the global optimizer required a complete gradient-based sizing optimization at the inner level. Now, each infill point requires 12 such gradient-based optimizations: one for each of the 12 LHS sample points needed to construct the PCE. The 12 LHS sample points can then be used to compute the mean structural mass (μ_f) and the standard deviation (σ_f), which are then returned to the surrogate optimizer. Each of these 12 sizing optimizations can, of course, be conducted in parallel.

The algorithmic steps are as follows. The vector of random variables, $\boldsymbol{x}_{random}$, consists of k_s and k_b.

1. Generate an initial population of $\boldsymbol{x}_{topology}$ designs using LHS.

8

2. For each topological design, generate a second LHS population across the $\boldsymbol{x}_{random}$ space. For each member of $\boldsymbol{x}_{random}$ (and for a fixed $\boldsymbol{x}_{topology}$), conduct the complete gradient-based optimization of $\boldsymbol{x}_{sizing}$, and return the optimal structural mass.

3. Use the PCE-based formulas to compute μ_f and σ_f for each topology, and compute the final objective function $\bar{f} = (1 - w) \cdot \mu_f + w \cdot \sigma_f$ for each topology, where w is some predetermined weighting factor.

4. Fit $\bar{f}$ with a radial basis function (RBF) surrogate model across the $\boldsymbol{x}_{topology}$ design space.

5. Use the surrogate model to find an infill point: i.e., the next topological design worth exploring.

6. For the new $\boldsymbol{x}_{topology}$ infill point, again generate a LHS population across the $\boldsymbol{x}_{random}$ space, conduct sizing optimization for each $\boldsymbol{x}_{random}$ member, and use PCE to compute $\bar{f}$.

7. Recompute the surrogate model with this new data point included.

8. Return to step 5, and repeat until a convergence criteria is attained.

If w is set to 0, the nested optimizer will minimize the mean structural mass, a result which is expected to closely resemble the deterministic optimization in Fig. 3: the deterministic sizing and the PCE-based average sizing results seen thus far are quantitatively similar. If w is set to 1, however, we will obtain a topology that minimizes the standard deviation, and is therefore more robust in the face of uncertain SF. This robustness will likely come at the cost of heavier average structural mass (and deterministic structural mass). For this work, the complete trade-off (Pareto front) is generated by running 11 optimizations: w set to 0, 0.1, ..., 0.9, 1.0. Each infill point for each of these 11 optimizations can then be gathered into a single set, and the final Pareto front between μ_f and σ_f can be obtained. This result is shown in Fig. 9.
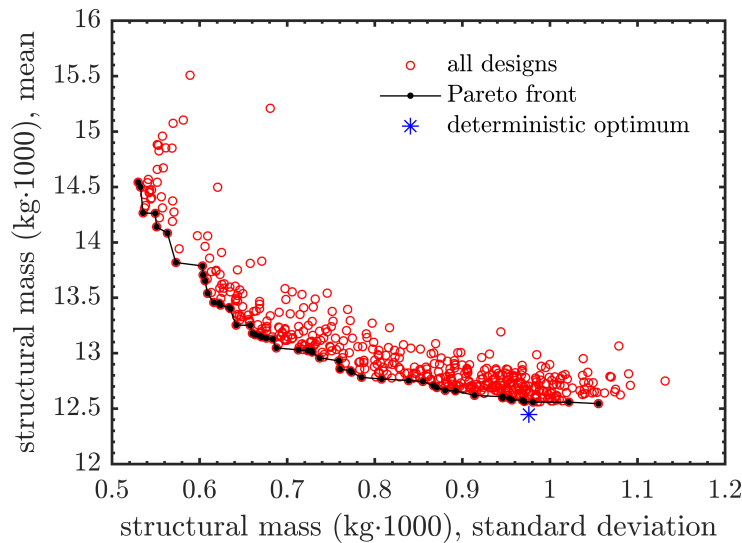

Figure 9: Pareto front between mean structural mass and standard deviation.

The topology with the best average structural mass (i.e., minimum μ_f, right-most extreme on the Pareto front in Fig. 9) has a mean mass of 12,544 kg and standard deviation of 1055 kg. This is comparable to the stochastic results found from the deterministic optima, as expected. The deterministic optima is superior to the results on the Pareto front in Fig. 9, in fact, indicating that the Pareto front is not completely converged within the $\boldsymbol{x}_{topology}$ space: further nested optimization iterations should push the Pareto front to lie through the deterministic data point seen in the figure. The topology with the lowest standard deviation (i.e., minimum σ_f, left-most extreme on the Pareto front in Fig. 9) has a mean structural mass of 14,542 kg, and standard

deviation of only 529 kg. These two extremes indicate that the standard deviation can be halved, but at the expense of a 16%-heavier nominal structural mass.

The topologies at the extremes of the Pareto front are shown in Fig. 10, where the key topological shifts for improved robustness (i.e., lower standard deviation) include fewer skin stiffeners, a forward rotation of those stiffeners (a known strategy for passive load alleviation during static aeroelastic maneuver loads [19]), and a decreased rib pitch near the wing break. The corresponding structural mass PDFs are also shown in this figure; the PDF for the robust design has very low skewness compared to the topology that minimizes the mean structural mass, indicating a more linear Gaussian process.
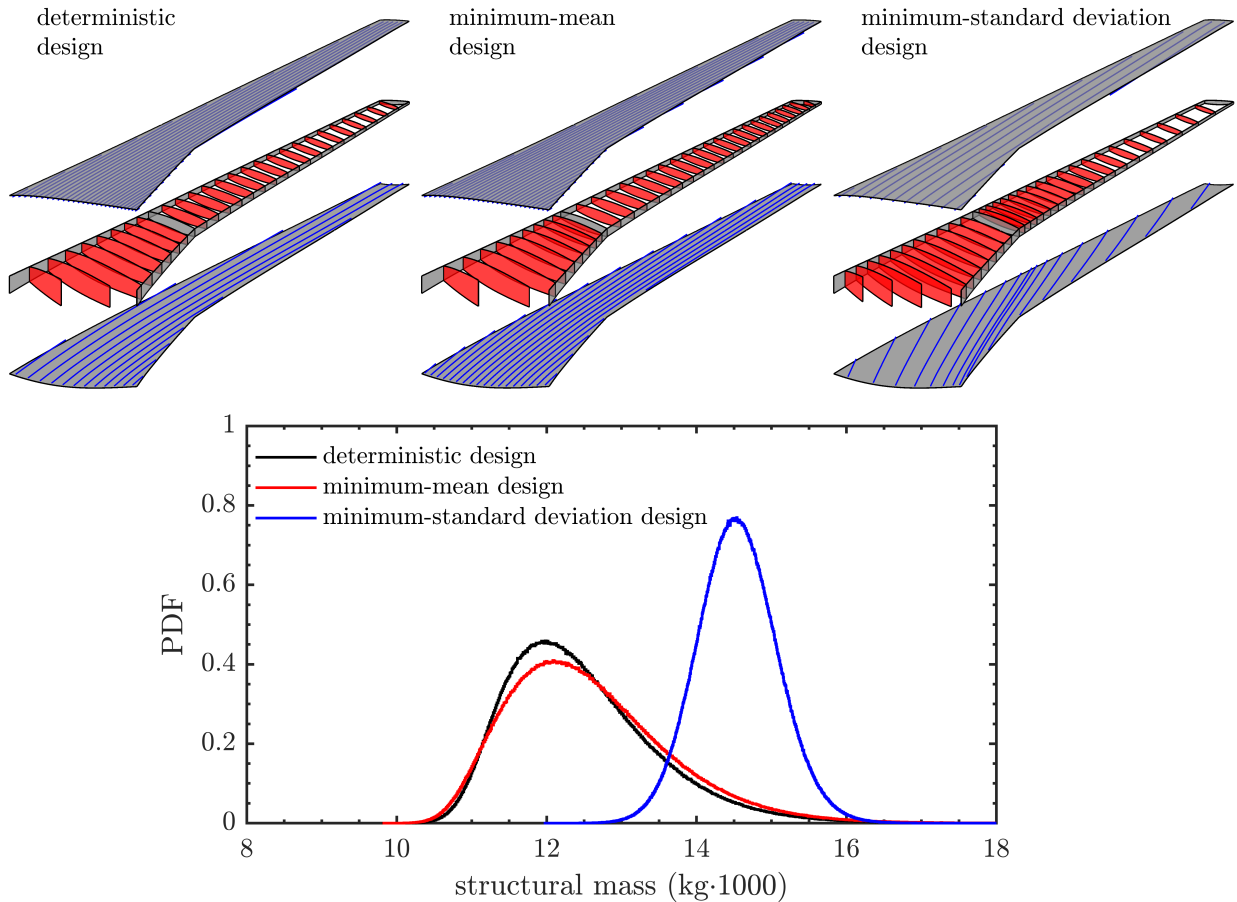

Figure 10: Topologies and structural mass PDFs at the extremes of the Pareto front, as well as the deterministic result.

Additional insight into the key design trends across the Pareto front of Fig. 9 can be seen in Fig. 11 and Fig. 12. Figure 11 plots the variation of some of the topological design variables across the Pareto front (the number of ribs, the number of stringers, and the rotation of the stringers), specifically plotted as a function of σ_f. Though general trends are largely observable, some noise is seen across these plots, which may be attributed to various factors: 1), the inherent noise across the $x_{topology}$ design space, which is the original motivation for using a surrogate-based global optimizer for these design variables, as opposed to a gradient-based optimizer, and 2), the stochastic nature of the global optimizer, where the CP method used to compute infill points [13] relies on some random computations. Further convergence of the nested optimization process may be expected to decreases the noise associated with point 2,

and as already demonstrated in Fig. 9, the Pareto front computed here is slightly inferior to known optima in some locations (namely, at the deterministic data point), indicating room for additional convergence.
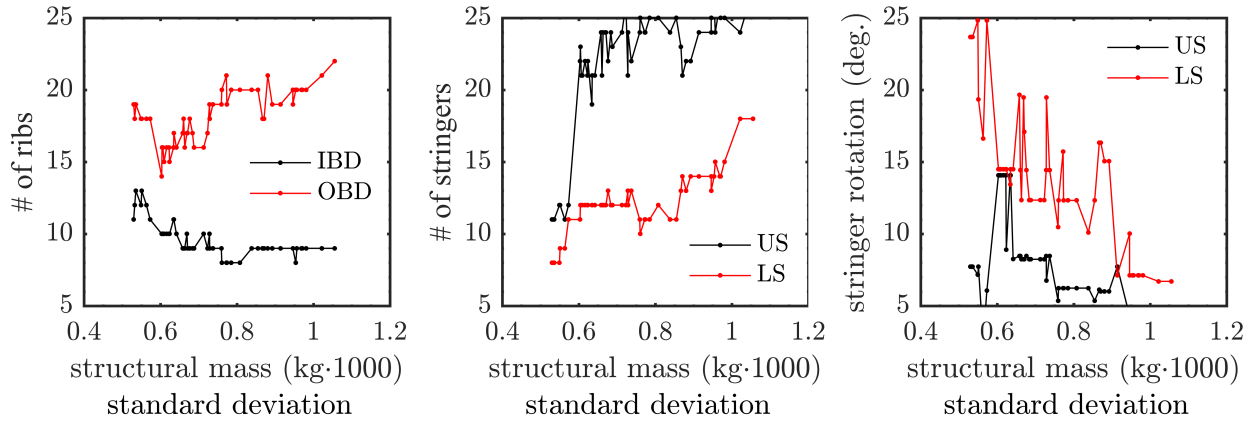

Figure 11: Variation in component topology across the Pareto front of Fig. 9: inboard (IBD) and outboard (OBD) ribs, upper skin (US) and lower skin (LS) stringers.

Figure 12 shows the PCE fitting error (namely, the root mean square error, RMSE) across the Pareto front. No discernible trend is seen here, with fitting errors on the order of 10-40 kg of structural mass. This lack of trend is perhaps surprising, given that the less robust designs (i.e., those with higher standard deviations) demonstrate marked nonlinearity in the PDF shape, as also evidenced by skewness and kurtosis trends in Fig. 12. The designs with lower standard deviations approach skewness and kurtosis levels on par with normal Gaussian processes (i.e., 0.0 skew and 3.0 kurtosis).
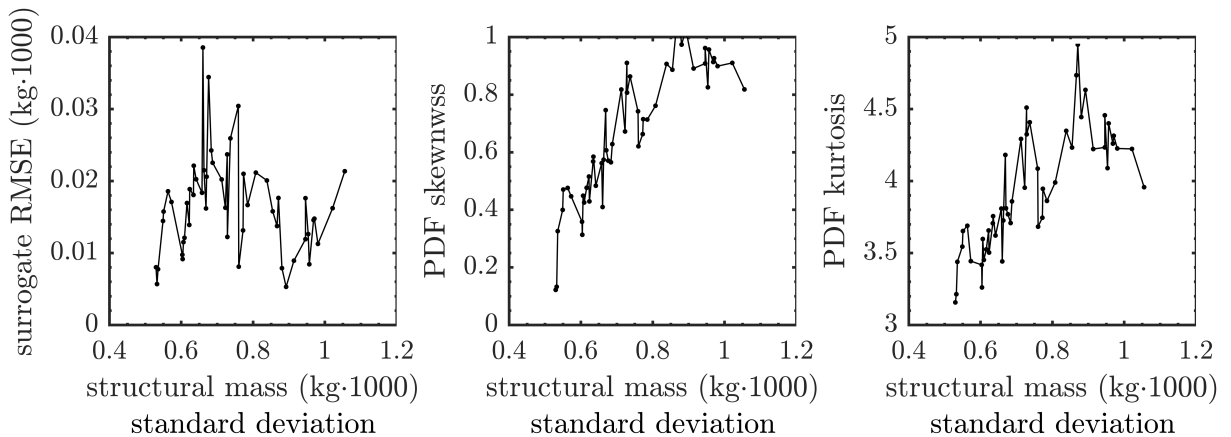

Figure 12: Variation in fitting error (left), PDF skewness (center), and PDF kurtosis (right) across the Pareto front of Fig. 9.

The final result shown here is the Sobol indices across the Pareto front, in Fig. 13. These indices, which are global nonlinear sensitivity parameters, can be computed analytically from the PCE expansion [20], and provide insight into the relative importance of each random variable. The results shown in this figure are surprising: for the robust designs with low standard deviation, the random safety factors k_s and k_b are of roughly equal importance. For designs on the other

11

end of the Pareto front, however, the Sobol index associated with the buckling safety factor drops to 0, and the index associated with stress rises to 1 (i.e., k_b is of no importance relative to k_s). This is surprising in the sense that the buckling constraint is active during the gradient-based sizing optimization, for every design across the front (for each of the 4 aeroelastic load cases), including the low-μ_f designs for which the buckling Sobol index is 0.

Of course, the degree to which a design constraint is active may vary, and the results of Fig. 13 indicate that, for the designs near the extreme right of the Pareto front, the Lagrange multipliers associated with the buckling constraint are small compared with the stress constraint, though not exactly zero (i.e., the buckling constraints are active, but weak). Therefore, the fundamental strategy pursued by the nested optimizer in order to improve robustness (i.e, decrease standard deviation) in the face of uncertain safety factors is to shift the wingbox topology in a way that increases the importance of the buckling constraint to be on-par with the stress constraint.
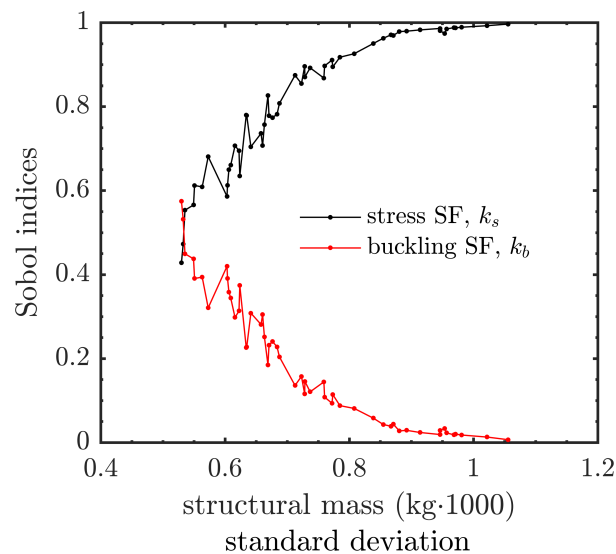

Figure 13: Variation in Sobol indices across the Pareto front of Fig. 9.

5 CONCLUSIONS

This work has considered a nested optimization procedure for simultaneous sizing and topological layout design of an aeroelastic wingbox. The inner level of the nested procedure handles the sizing optimization (i.e., the thickness of the skin panels) via adjoint-driven gradient-based optimization, whereas the outer level handles the topology design (i.e., the number and placement of the skin stringers). The sizing optimization is driven by a series of stress and buckling constraints spread across several trimmed maneuvers, and the safety factors associated with stress and buckling are considered to be stochastic, with an assumed probability distribution. A nonintrusive polynomial chaos expansion is used to propagate the uncertainties through the aeroelastic system. The objective function of the complete optimization process is to minimize some linear combination of the mean and the standard deviation of the structural mass; designs that minimize the latter will be more robust in the face of uncertainties in the safety factors.

Topological designs that minimize the mean structural mass are found to be largely similar to designs obtained deterministically, which simply minimize the nominal structural mass. The PDFs in structural mass for these designs are fairly skewed, justifying the use of a second-order (i.e., nonlinear) PCE. Minimizing the standard deviation, on the other hand, decreases

the standard deviation by nearly half, at the expense of a 16% increase in the average/nominal structural mass. The PDFs for these designs are largely linear, with skewness near zero. The topological shifts needed to improve robustness involve decreasing the number of stiffeners, rotating the stiffeners ahead of the leading edge (namely in the lower skins), and shifting a number of ribs from the outboard wing section to the inboard section. A Sobol sensitivity analysis indicates that the improvements in robustness are accompanied by an increase in the importance level of the buckling constraints, relative to the stress constraints.

6 REFERENCES

[1] Stanford, B., Jutte, C., Coker, C., "Aeroelastic Sizing and Layout Design of a Wingbox through Nested Optimization," *AIAA Journal*, Vol. 57, No. 2, pp. 848-857, 2018.

[2] Roy, S., Crossley, W., Stanford, B., Moore, K., Gray, J., "A Mixed Integer Efficient Global Optimization Algorithm with Multiple Infill Strategy - Applied to a Wing Topology Optimization Problem," AIAA Paper 2019-2356, 2019.

[3] Brooks, T., Kenway, G., Martins, J., "Benchmark Aerostructural Models for the Study of Transonic Aircraft Wings," *AIAA Journal*, Vol. 56, No. 7, pp. 2840-2855, 2018.

[4] Hansen, L., Horst, P., "Multilevel Optimization in Aircraft Structural Design Evaluation," *Computers and Structures*, Vol. 86, No. 1, pp. 104-118, 2008.

[5] Wang, W., Guo, S., Yang, W., "Simultaneous Partial Topology and Size Optimization of a Wing Structure Using Ant Colony and Gradient Based Methods," *Engineering Optimization*, Vol. 43, No. 4, pp. 433-446, 2011.

[6] Jrad, M., De, S., Kapania, R., "Global-Local Aeroelastic Optimization of Internal Structure of Transport Wing," *AIAA Multidisciplinary Analysis and Optimization Conference*, Denver, CO, June 5-9, 2017.

[7] Müller, J., "MISO: Mixed Integer Surrogate Optimization Framework," *Optimization and Engineering*, Vol. 17, No. 1, pp. 177-203, 2016.

[8] Yao, W., Chen, X., Luo, W., van Tooren, M., Guo, J., "Review of Uncertainty-Based Multidisciplinary Design Optimization Methods for Aerospace Vehicles," *Progress in Aerospace Sciences*, Vol. 47, No. 6, pp. 450-479, 2011.

[9] Beran, P., Stanford, B., Schrock, C., "Uncertainty Quantification in Aeroelasticity," *Annual Review of Fluid Mechanics*, Vol. 49, pp. 361-386, 2017.

[10] Elishakoff, I., "Uncertain Buckling: its Past, Present, and Future," *International Journal of Solids and Structures*, Vol. 37, pp. 6869-6889, 2000.

[11] Elishakoff, I., *Safety Factors and Reliability, Friends or Foes?*, Kluwer Academic Publishers, the Netherlands, 2004.

[12] Qu, X., Haftka, R., "Reliability-Based Design Optimization using Probabilistic Sufficiency Factor," *Structural and Multidisciplinary Optimization*, Vol. 27, pp. 314-325, 2004.

[13] Regis, R., Shoemaker, C., "Combining Radial Basis Function Surrogates and Dynamic Coordinate Search in High Dimensional Expensive Black-Box Optimziation," *Engineering Optimization*, Vol. 45, No. 5, pp. 529-555, 2013.

[14] Kreisselmeier, G., Steinhauser, R., "Systematic Control Design by Optimizing a Vector Performance Index", *International Federation of Active Controls Symposium on Computer-Aided Design of Control Systems*, Zurich, Switzerland, 1979.

[15] Hosder, S., Walters, R., Balch, M., "Point-Collocation Nonintrusive Polynomial Chaos Method for Stochastic Computational Fluid Dynamics," *AIAA Journal*, Vol. 48, No. 12, pp. 2721-2730, 2010.

[16] Eldred, M., "Recent Advances in Non-Intrusive Polynomial Chaos and Stochastic Collocation Methods for Uncertainty Analysis and Design," AIAA Paper 2009-2274.

[17] Lansing, W., Dwyer, W., Emerton, R., Ranalli, E., "Application of Fully Stressed Design Procedures to Wing and Empennage Structures," *Journal of Aircraft*, Vol. 8, No. 9, pp. 683-688, 1971.

[18] Scarth, C., Cooper, J., Weaver, P., Silva, G., "Uncertainty Quantification of Aeroelastic Stability of Composite Plates using Lamination Parameters," *Composite Structures*, Vol. 116, pp. 84-93, 2014.

[19] Williams, J., "Analysis/Theory of Controlled Configured Structures," AFFDL-TR-74-137, Air Force Flight Dynamics Laboratory, 1974.

[20] Sudret, B., "Global Sensitivity Analysis using Polynomial Chaos Expansion," *Reliability Engineering and System Safety*, Vol. 93, No. 7, 2008, pp. 964-979.

COPYRIGHT STATEMENT